Advanced Functional Materials

ADVANCED FUNCTIONAL MATERIALS
www.afm-journal.de

RESEARCH ARTICLE

High-Performance Color Printing and Information Encryption Enabled by Silicon Carbide Metasurface

Yongze Ren[1] | Renchao Jin[1] | Maowen Song[1,2] | Peicheng Lin[1] | Ting Xu[1,2] | Yan-qing Lu[1,2]

[1]National Laboratory of Solid-State Microstructures, College of Engineering and Applied Sciences and Collaborative Innovation Center of Advanced Microstructures, Nanjing University, Nanjing, China | [2]Key Laboratory of Intelligent Optical Sensing and Manipulation, Ministry of Education, Nanjing University, Nanjing, China

Correspondence: Maowen Song (smw@nju.edu.cn) | Ting Xu (xuting@nju.edu.cn) | Yan-qing Lu (yqlu@nju.edu.cn)

Received: 30 September 2025 | **Revised:** 24 January 2026 | **Accepted:** 22 April 2026

Keywords: color printing | metasurface | polarization | silicon carbide | structural colors

ABSTRACT

Structural colors are central to high-fidelity printing and advanced displays, offering durable and accurate reproduction of visual information. Metasurfaces provide a powerful route to customize such colors, yet most efforts have been limited to tuning one or two parameters of the hue–saturation–brightness (HSB) space. Achieving comprehensive, simultaneous, and polarization-independent control of HSB remains a critical challenge. Here, we present an ultrathin monolithic silicon carbide (SiC) metasurface that enables independent and simultaneous modulation of the entire HSB color space, while also supporting robust optical information encryption. The metasurface realizes HSB color nanoprinting with chiaroscuro effects, facilitating the encoding of complex visual hierarchies. Moreover, by modulating the polarization state of incident light, two distinct images can be selectively revealed or concealed with minimal crosstalk. The device further achieves printing resolutions exceeding 10 000 pixels per inch (PPI), highlighting its potential for next-generation displays, imaging systems, and secure data storage.

1 | Introduction

Color is a fundamental element of human visual perception and serves as a critical channel for information transfer [1, 2]. Conventional dyes and pigments, which generate color through wavelength-selective absorption and reflection [3, 4], are commonly used in our daily applications but suffer from chemical instability, limited color gamut, and micron-scale resolution, restricting their use in advanced display technologies. By contrast, structural colors—arising from light–matter interactions—offer superior advantages, including resistance to fading, environmental sustainability, and subwavelength resolution [5–7].

Metasurfaces, comprising arrays of artificial subwavelength nanostructures, provide an unprecedented platform for tailoring electromagnetic waves [8–11]. These devices have enabled diverse applications such as structural color imaging [12–27], polarimetry [28–31], optical data storage [32–34], and structured light generation [35–39]. Structural color metasurfaces are generally categorized as plasmonic or dielectric platform. Plasmonic metasurfaces, typically based on metallic nanodisks, nanoholes, or metal–insulator–metal nanopillars [4, 12–17], can achieve high spatial resolution and wide color gamut. However, they are usually composed by lossy, expensive metals, which limit color saturation and brightness. Although cross-polarization conversion can effectively solve this problem [40],

Yongze Ren and Renchao Jin contributed equally to this work.

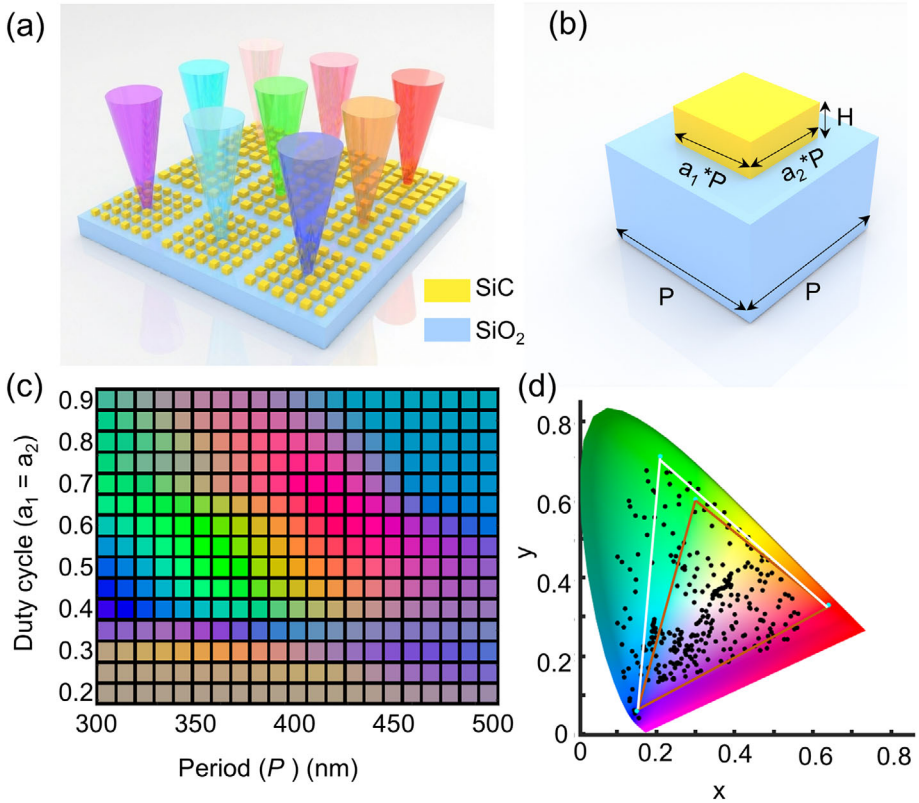

FIGURE 1 | Schematic of the proposed SiC metasurface. (a) Schematic diagram of the SiC metasurface, which comprises periodic arrangements SiC nanobricks located on a fused silica substrate. (b) Perspective view of unit cell that contains a SiC nanobrick with a period of P. The duty cycles along the x and y axes are represented by a_1 and a_2. The height of the SiC nanobrick is fixed at $H = 120$ nm. (c) The simulated color palette as a function of both the period and the duty cycle of the SiC nanobricks array. (d) The corresponding CIE chromaticity coordinates of the colors in Figure 1c. The orange and white regions represent the sRGB and Adobe RGB color gamut, respectively.

the approach requires external analyzers and suffers from relatively low efficiency. Dielectric metasurfaces have emerged as a compelling alternative. By exploiting Mie resonances in lower loss materials such as silicon (Si) [18–20], silicon nitride (Si_3N_4) [21–23], and titanium dioxide (TiO_2) [24–26], sharp spectral responses can be engineered across the visible range by tuning nanopillar morphology and geometry. Despite these advantages, most dielectric metasurfaces address one or two parameters of the HSB space, leaving brightness modulation largely unexplored. This limitation hinders their capabilities for chiaroscuro imaging and high-fidelity display.

Several strategies have been proposed to overcome this challenge. Bao et al. demonstrated hue–saturation–brightness (HSB) modulation via diatomic interference in Si nanopillars [41], but their approach required extreme aspect ratios (~1:15) and yielded a restricted color gamut. Brightness tuning has also been realized using in-plane geometric variations of silver nanorods, where near-field coupling modulates reflectance intensity [14]. However, this method provides limited reflectance and only ~55% coverage of the sRGB color gamut. TiO_2-based metasurfaces employing Malus's law can achieve continuous amplitude modulation [42], yet their reliance on external analyzers and low-quality-factor resonances prevents reproduction of high-saturation colors. Similarly, surface-relief silver metasurface for high-performance color generation [43] requires polarizer–analyzer pairs, further complicating integration into compact systems.

Here, we introduce an ultrathin dielectric metasurface composed of silicon carbide (SiC) nanobricks that overcomes these limitations. SiC combines a high refractive index with low loss, enabling high color saturation, wide gamut coverage, chiaroscuro rendering, and polarization-dependent tunability across the visible spectrum. Experimentally, we achieve 154% coverage of the sRGB color gamut and continuous brightness modulation by tailoring the geometry and filling factor of the nanobricks within each unit cell. Our approach extends traditional hue–saturation (HS) control to full HSB modulation without the assistance of external analyzer. In addition, the intrinsic birefringence of anisotropic SiC nanobrick allows polarization-dependent encoding of two distinct images with minimal cross-talk effect. The metasurface is fabricated without high-aspect-ratio etching and supports ultrahigh-resolution (~10 000 PPI) nanoprinting. Consequently, such SiC metasurface offers a promising platform for next-generation high-performance displays, secure optical encryption, and multifunctional photonic devices.

2 | Results and Discussions

Figure 1a illustrates the proposed dielectric metasurface, consisting of a periodic array of SiC nanobricks on a fused silica

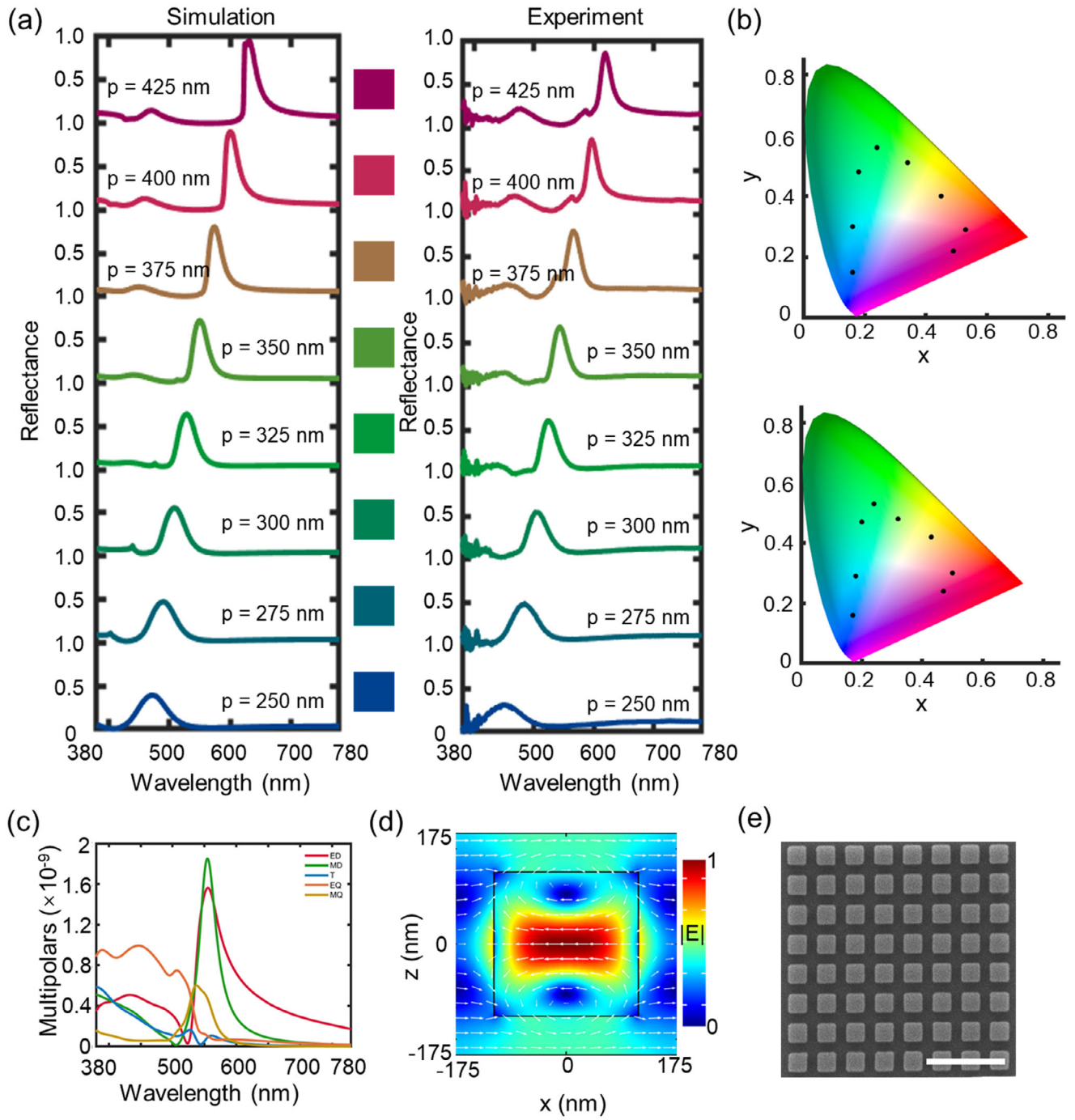

FIGURE 2 | Experimentally measured spectra and fundamental mechanism of the SiC metasurface. (a) Simulated (left panel) and measured (right panel) reflection spectra with the increasing period ranging from 250 to 425 nm, respectively. The corresponding calculated color (middle panel) from simulated spectra. (b) Simulated (top) and experimental (bottom) CIE 1931 chromaticity coordinates based on reflectance spectra in Figure 2a. (c) Multipolar decomposition of scattering cross-sections in terms of ED, MD, T, EQ, and MQ, respectively. The geometry parameters of selected SiC unit cell has a period of $P = 350$ nm and a duty cycle of 0.65. (d) Electric field profile at the resonant wavelength of 548 nm, and the white arrows denoting the field direction. (e) The SEM image of the fabricated SiC metasurface. Scale bar: 1 μm.

substrate. This platform is compact, CMOS-compatible, and optimized for high-performance structural color generation. SiC is selected for its high refractive index and low optical loss across the visible spectrum. A comparison of its optical constants with those of TiO_2, Si_3N_4, and Si is provided in Section S1. Each nanobrick is defined by its period P and duty cycles a_1 and a_2 along the x and y axes, respectively, as shown in Figure 1b. The height of the nanobrick is fixed at H = 120 nm, yielding a low aspect ratio that simplifies fabrication and enhances scalability. By tuning the period and duty cycles, Mie resonances can be shifted across the visible spectrum, resulting in full-color output as illustrated in Figure 1c. Mapping onto the CIE 1931 diagram depicted in Figure 1d shows a color gamut covering 166% of sRGB and 115% of Adobe RGB, outperforming many reported

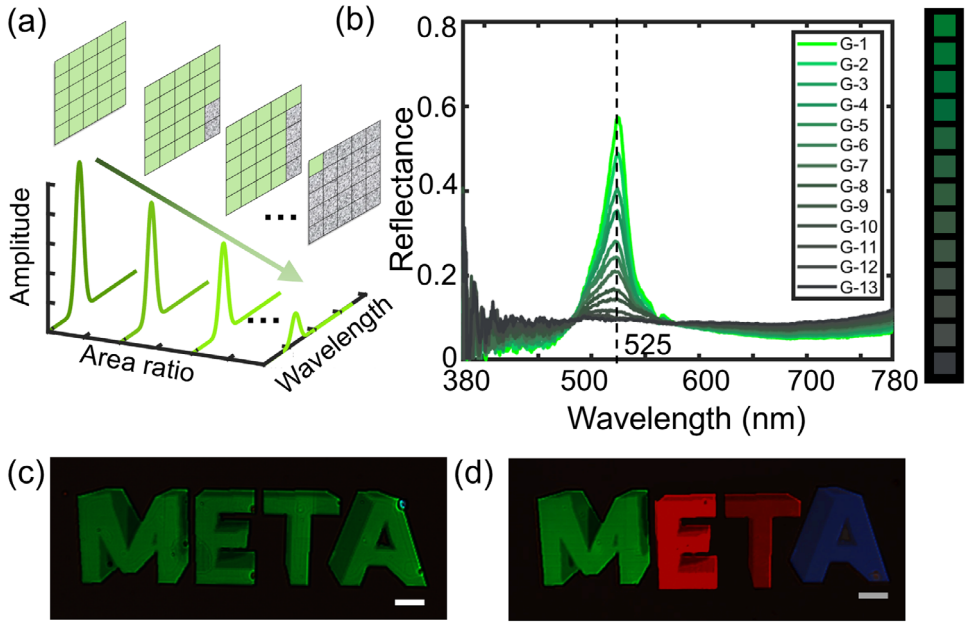

FIGURE 3 | Schematic diagram of brightness modulation. (a) Principle of amplitude modulation realized by adjusting the areal ratio of SiC nanobricks within a 5 μm × 5 μm unit area. The gray regions represent the areas without SiC nanobricks. (b) Experimental reflectance spectra for different SiC area ratios, labeled by G-1–G-13, along with the corresponding colors derived from each spectrum. (c) Experimental results of structural color patterns generated from a single hue with brightness modulation. (d) Experimental multicolor images with brightness modulation. Scale bar: 100 μm.

approaches (Section S2). The color gamut of structural colors can be further expanded by introducing refractive index matching layers to suppress higher-order resonant modes. In addition, inverse design strategies could be used to optimize the structural geometries and dimensions.

To evaluate performance, Finite-Difference Time-Domain (FDTD) simulations were performed with periodic boundary conditions along the x and y axes and perfectly matched layers along the z direction. The optical parameters of SiC used in simulation were obtained by ellipsometry (Figure S1). Figure 2a showcases that each simulated reflection spectrum exhibits a sharp peak, which redshifts from 472 to 664 nm as the period increases from 250 to 425 nm, with an average efficiency of 78.4%. The duty cycles of which are fixed to 0.65. Experimentally measured spectra shown in the right panel of Figure 2a exhibit similar trends but slightly lower efficiency (69%). These discrepancies can be attributed to the following reasons: (i) fabrication imperfections that cause deviations in the morphology of the fabricated SiC nanobricks; (ii) differences in the material parameters between the simulation model and the fabricated metasurface. The corresponding colors, derived from CIE color-matching functions, are shown in the middle panel of Figure 2a. Figure 2b presents good agreement between simulated and experimental chromaticity plots, with experimental coverage of 154% sRGB and 107% Adobe RGB (Figure S2) in the CIE diagram.

In order to have a better understanding of the underlying mechanism, multipole scattering theory [44] was applied to a representative unit cell ($P = 350$ nm, $a_1 = a_2 = 0.65$). The total scattering cross section can be decomposed into contributions from various multipolar modes, including the electric dipole (ED), magnetic dipole (MD), toroidal dipolar (T), electric quadrupole (EQ), and magnetic quadrupole (MQ), as the following form:

$$\mathrm{I} = \frac{2\omega^4}{3c^3}|P|^2 + \frac{2\omega^4}{3c^3}|M|^2 + \frac{4\omega^5}{3c^4}(P \cdot T) + \frac{2\omega^6}{3c^5}|T|^2 + \frac{\omega^6}{5c^5}Q_{\alpha\beta}Q_{\alpha\beta} + \frac{\omega^6}{20c^5}M_{\alpha\beta}M_{\alpha\beta} + \frac{2\omega^6}{15c^5}\left(M \cdot \left\langle R_M^2 \right\rangle\right) + o\left(\frac{1}{c^5}\right) \quad (1)$$

where c represents the speed of light in vacuum, ω represents the angular frequency. $\boldsymbol{P}$, $\boldsymbol{M}$, $\boldsymbol{T}$, $Q_{\alpha\beta}$, $M_{\alpha\beta}$ represent the ED, MD, T, EQ, and MQ moments, respectively. $\langle R_M^2 \rangle$ is the correction resulting from the interference between the MD and first-order mean-square radius of the MD distribution (see details in Section S3).

Figure 2c shows the multipole expansion under x-polarized illumination. A strong resonance peak emerges at 548 nm, consistent with the primary reflection peak. The scattering is dominated by the MD resonance, overlapping with the ED response. Notably, this spectral overlap suppresses multiple peaks, thereby preserving color purity. The corresponding electric field distribution at the resonant wavelength is plotted in Figure 2d, revealing strong field confinement inside the SiC nanobrick and a ring-shaped profile characteristic of MD modes, further presented by the magnetic field distribution as shown in Figure S3. These observations agree well with the multipole decomposition analysis. A scanning electron micrograph (SEM) of the fabricated SiC metasurface is shown in Figure 2e, with fabrication details provided in the Methods section.

To achieve brightness control, we varied the areal coverage of nanobricks within each individual unit cell as illustrated

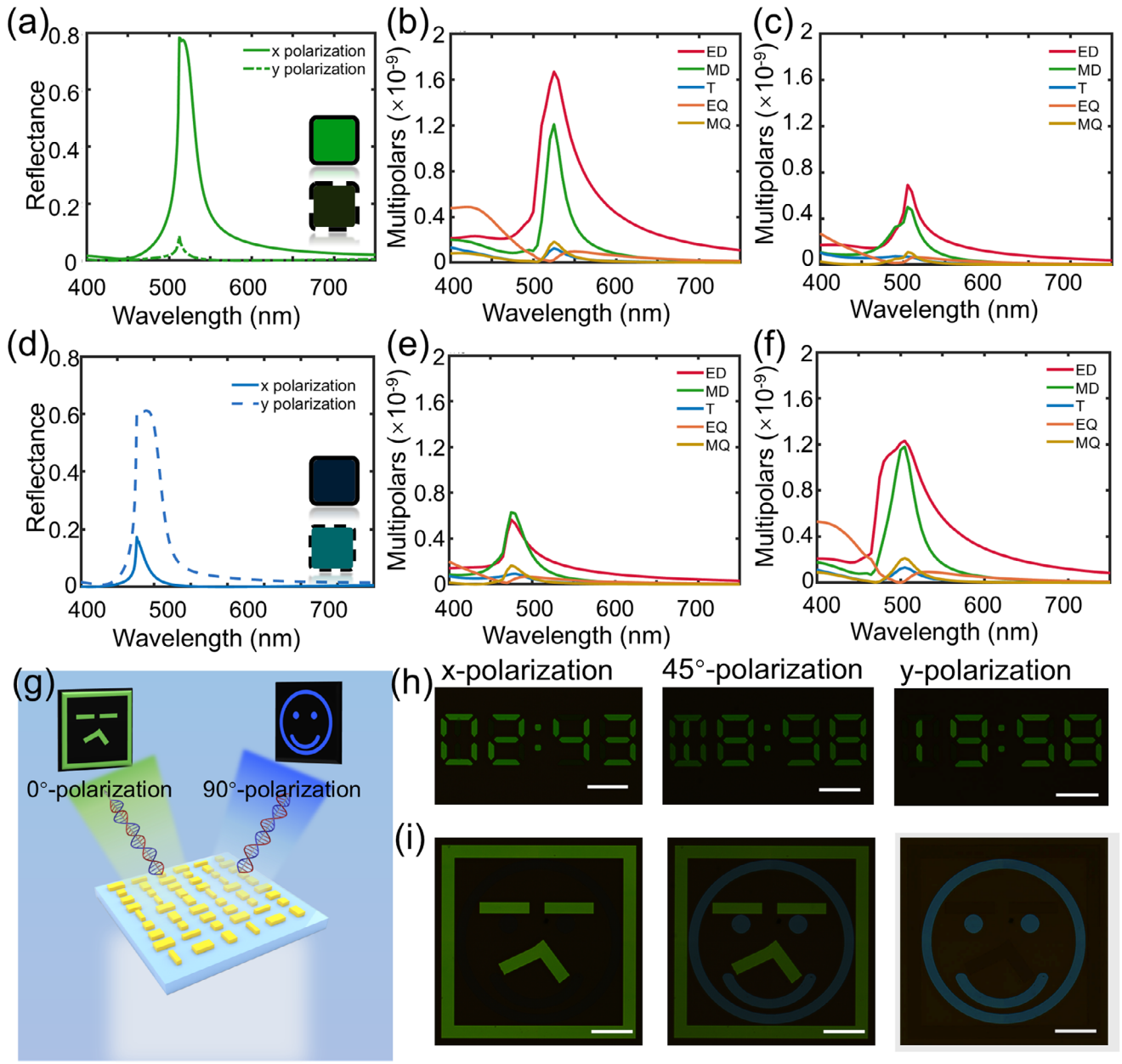

FIGURE 4 | Polarization-tunable performance of the SiC metasurface. (a) Simulated reflectance spectra under *x*- (green solid line) and *y*- (green dashed line) polarized light for a selected structure with a period of $P = 350$ nm and duty cycles of $a_1 = 0.65$ and $a_2 = 0.35$. The insets show the corresponding derived color for *x* (solid box) and *y* (dashed box) polarizations. (b,c) presents corresponding multi expansion for x and y polarization. (d) Simulated reflectance spectra under *x*- (green solid line) and *y*- (green dashed line) polarized light for a SiC nanobrick with a period of $P = 325$ nm and duty cycles of $a_1 = 0.65$ and $a_2 = 0.35$. The insets illustrate the corresponding derived color under *x*- (solid box) and *y*- (dashed box) polarized light. (e,f) presents corresponding multi modes expansion for x and y polarization. (g) Schematic illustration of polarization-controlled information storage. Experimental results of single color (h) and multicolor (h) switching under *x* (left), 45° (middle) and *y* (right) polarization states. Scale bar: 100 μm.

in Figure 3a. A 5 × 5 μm^2 region was divided into grids, and nanobrick coverage was gradually reduced by sequentially removing 1 × 2 μm^2 sub-regions, yielding 13 distinct patterns as depicted by optical micrographs in Figure S4. This approach smoothly modulates reflectance from 58% to 8% at 525 nm, producing colors from deep green to dark gray as shown in Figure 3b. As the area ratio of SiC nanobricks decreases, the resulting reflected color gradually reduces and approaches that of the bare quartz substrate, making it difficult to achieve a true black state in practical displays. Although the reflectance cannot be decreased to zero, broadband reflection with ~8% reflectance is comparable to some unbonded glass used in a display device. In addition, the reflectance could be further decreased to zero by adding additional polarizers or using liquid crystal layers. Unlike cross-polarization or interference methods, this approach requires no additional polarizer, resulting in simplicity and high compatibility. Brightness modulation at fixed hue enables realistic chiaroscuro effects, as demonstrated by the "META" pattern in Figure 3c. The brightness contrast produces a vivid 3D appearance, whereas absent of brightness information

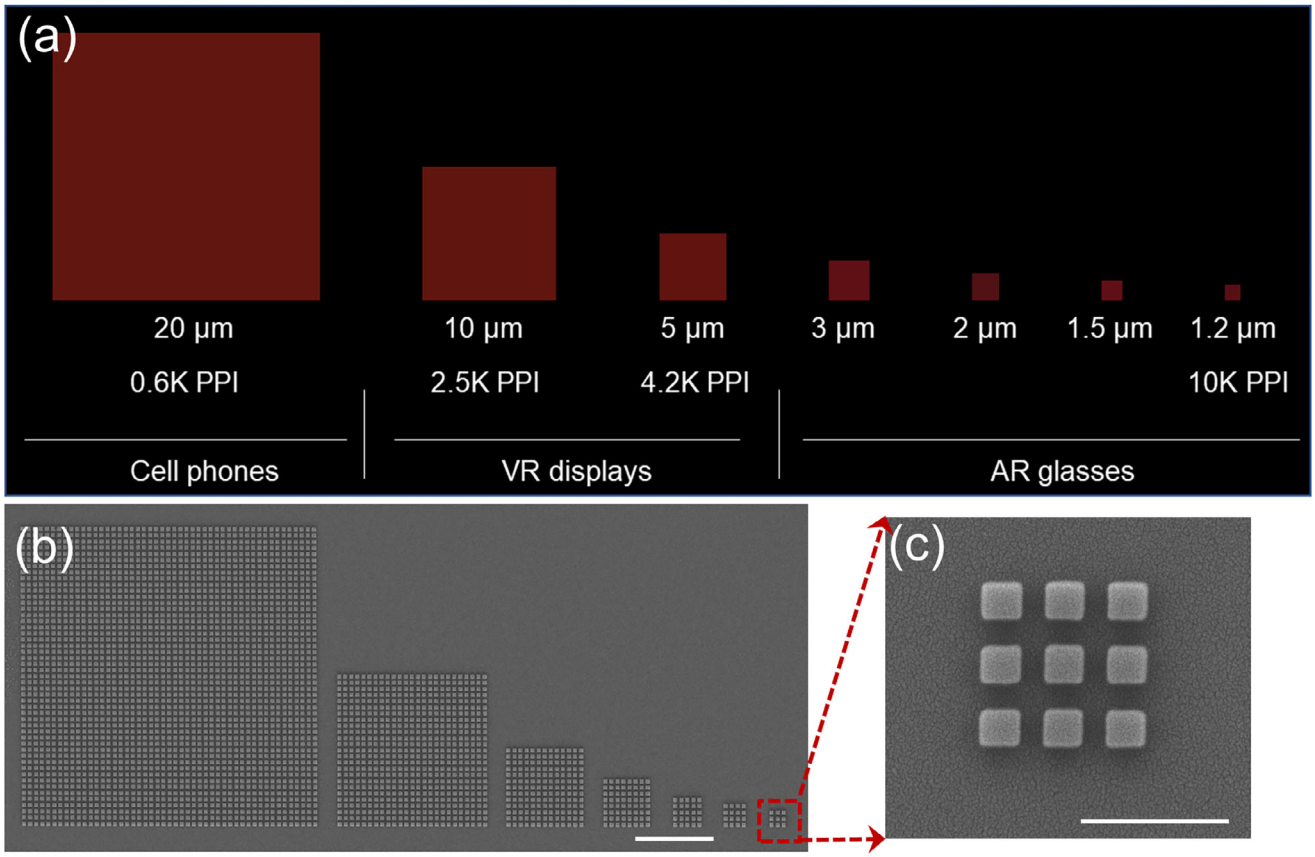

FIGURE 5 | Resolution test of the SiC metasurface. (a) Optical micrograph of SiC nanobricks with various sizes changing from 20 to 1.2 μm. The geometry parameters of the corresponding SiC nanobricks have a period of $P = 410$ nm and duty cycles of $a_1 = a_2 = 0.6$. (b) SEM images of SiC nanobricks corresponding to Figure 5a, scale bar 5 μm. (c) The magnified part in Figure 5b, scale bar 1 μm.

yields a flat, monochromatic pattern. Similar demonstrations for red, orange, and blue patterns are shown in Figure 3d,e. The corresponding experimental setup is shown in Figure S5.

Beyond color hue and brightness modulation, the birefringence of anisotropic SiC nanobricks for polarization-dependent color switching is exploited. Without changing material composition or geometry, polarization provides an additional degree of freedom for color tuning, increasing information capacity stored in each individual color pixel. Figure 4a shows that a structure with $P = 350$ nm, $a_1 = 0.65$, and $a_2 = 0.35$ exhibits vivid green (78% reflectance) under x polarization while vanished color (8% reflectance) under y polarization. Multipole decomposition presented in Figure 4b,c reveals a dominant ED resonance under x polarization and a strongly suppressed ED response under y polarization, consistent with the anisotropic geometry. The corresponding electric and magnetic field distributions (Figure S6) confirm the polarization-dependent field confinement modes. A second design with $P = 325$ nm and duty cycles of 0.35 and 0.65 switches between black (x polarization) and cyan-blue (y polarization) as shown in Figure 4d, which is consistent with multipole and field analyses provided in Figure 4e,f and Figure S7.

These polarization-dependent optical responses enable information encryption. As shown in Figure 4g, distinct encoded patterns are selectively revealed under orthogonal polarization states. Experimentally, the metasurface displays "02:43" under x-polarized illumination and "19:58" under y-polarized illumination (Figure 4h). Notably, negligible crosstalk between the two polarization channels is observed. When the incident polarization is rotated to 45°, destructive interference obscures the "time" information, broadly enhancing encryption robustness. In addition, the spatial multiplexing technique is demonstrated to encode distinct color images under orthogonal polarizations. To minimize crosstalk effect, the background was engineered using SiC nanobricks ($P = 410$ nm, duty cycles of 0.25) to produce a dark state under both polarizations, matching the backgrounds of Figure 4a (y polarization) and Figure 4d (x polarization). Using this scheme, a green "cry face" with sharp contrast appears under x polarization while a blue "smile face" presents under y polarization as shown in Figure 4i. The two channels are spectrally and spatially isolated, yielding negligible crosstalk effect. Polarization-dependent color palettes of various nanostructures are provided in Figure S8. Such multiplexing technique enriches polarization-encoded color diversity, offering a promising platform for encryption, anticounterfeiting, and advanced display technology.

Finally, the resolution of our SiC metasurface was tested by fabricating periodic nanobricks with pixel size from 20 down to 1.2 μm as shown in Figure 5a. It can be observed that the red color still exists even the pixel only consists of 3 × 3 nanobricks, corresponding to ultrahigh pixel densities of 10 000 PPI. Figure 5b,c

show the SEM images in which each SiC nanobrick exhibits high fidelity. Additional optical and SEM images for other color pixels can be seen in Figures S9 and S10.

3 | Summary

In this paper, we have demonstrated an ultrathin SiC-on-silica metasurface that simultaneously achieves wide-gamut color generation, brightness modulation, and polarization-dependent switching. Multipole decomposition theory confirms optical MD resonances as the primary mechanism that enables experimental gamut coverage of 154% sRGB and 107% Adobe RGB. Brightness is experimentally modulated via areal coverage engineering, supporting chiaroscuro rendering with high contrast. Polarization-dependent birefringence allows multiplexing images with minimal crosstalk effect. High-resolution nanoprinting up to 10 000 PPI further showcases the suitability of our SiC metasurfaces for next-generation displays, imaging, and optical encryption.

4 | Methods

4.1 | Optical Characterization

Optical images of the metasurface colors were captured using an inverted microscope (Zeiss Axio Observer) under broadband white light illumination. The optical photographs were obtained by a chromatic CCD camera (Zeiss AxioCam MRc5). An ultraviolet–infrared–near infrared microspectrophotometer (CRAIC PV20/30) was used to measure the reflectance spectrum.

4.2 | Fabrication of SiC Metasurface

The metasurfaces were fabricated by standard electron beam lithography and reactive ion etching technology (Figure S11). We first deposited 120-nm-thick silicon carbide using plasma-enhanced chemical vapor deposition (Oxford, PlasmaPro 100 PECVD) on a 500-μm-thick fused silica substrate. O_2 plasma cleaning and HMDS coating on silicon carbide film were executed to improve adhesion. Then, the 190-nm-thick positive electron-beam resist (PMMA) was spin-coated on the silicon carbide film. Subsequently, an E-spacer layer (ARPC5090) was spin-coated on the resist to suppress the charging effect. The designed patterns were defined in resist by an electron beam lithography system (Elionix, ELS-F125) and developed in the solution of MIBK and IPA. Next, a 28-nm-thick aluminum layer was deposited on the resist by an electron beam evaporator (SKY, DZS500) and a lift-off process was done in n-methyl-pyrrolidone (NMP) at 80°C. In order to transfer the patterns from the aluminum hard mask to the silicon carbide film, inductively coupled plasma reactive ion etching (Tailong Electronics, ICP-200) was carried out. C_4F_8 and SF_6 were utilized in the etching process, where the ratio of C_4F_8/SF_6 was tuned to be 2.6. The bias RF power was 40 W, the ICP generator RF power was 500 W, and the pressure was controlled at 13.5 mTorr. The etching time for the SiC film with a thickness of 120 nm was 60 s, corresponding to an etching rate of 120 nm/min. Finally, the metasurfaces composed of silicon carbide nanobricks were obtained after the removal of the aluminum layer with the stripping solution (Sigma–Aldrich, Aluminum Etchant Type A).

Author Contributions

Y.R. and M.S. conceived the idea. Y.R. and R.J. performed all the numerical simulations and imaging experiments. P.L. fabricated all the samples. Y.R. and M.S. conceived the color encryption concept and designed the experiment. Y.R. and M.S. wrote the article. M.S., T.X., and Y.L. supervised the project, discussed the progress and results, and edited the article.

Acknowledgements

We acknowledge support from the Key Research and Development Program of the Ministry of Science and Technology of China (2024YFB3614700 to M.S.), Jiangsu Provincial Frontier Research and Development Program (BF2025063 to M.S.), National Natural Science Foundation of China (62322507, 62475112 to M.S., 62305151 to R.J.), the Nanjing U35 Strong Foundation Project (to M.S.) and Fundamental Research Funds for the Central Universities (to M.S.).

Conflicts of Interest

The authors declare no conflicts of interest.

Data Availability Statement

The data that support the findings of this study are available on request from the corresponding author. The data are not publicly available due to privacy or ethical restrictions.

References

1. A. Kristensen, J. K. W. Yang, S. I. Bozheolnyi, et al., "Plasmonic Colour Generation," *Nature Reviews Materials* 2 (2017): 16088, https://doi.org/10.1038/natrevmats.2016.88.

2. I. C. Cuthill, W. L. Allen, K. Arbuckle, et al., "The Biology of Color," *Science* 357 (2017): aan0221, https://doi.org/10.1126/science.aan0221.

3. H. Zollinger, *Color Chemistry: Syntheses, Properties, and Applications of Organic Dyes and Pigments* (John Wiely & Sons, 2003).

4. M. Song, D. Wang, S. Peana, et al., "Colors With Plasmonic Nanostructures: A Full-spectrum Review," *Applied Physics Reviews* 6 (2021): 041308, https://doi.org/10.1063/1.5110051.

5. Z. Yan, Z. Zhang, W. Wu, et al., "Floating Solid-State Thin Films With Dynamic Structural Colour," *Nature Nanotechnology* 16 (2021): 795–801, https://doi.org/10.1038/s41565-021-00883-7.

6. S. D. Rezaei, Z. Dong, J. Y. E. Chan, et al., "Nanophotonic structural colors," *ACS photonics* 8 (2021): 18–33.

7. S. H. Choi, D. Kim, Y. Lee, et al., "Bioinspired Dynamic Colour Change," *Nature Reviews Bioengineering* 3 (2025): 579–595, https://doi.org/10.1038/s44222-025-00298-2.

8. N. Yu, P. Genevet, M. A. Kats, et al., "Light Propagation With Phase Discontinuities: Generalized Laws of Reflection and Refraction," *Science* 334, no. 6054 (2011): 333–337, https://doi.org/10.1126/science.1210713.

9. X. Zhang, X. Ji, X. Li, et al., "Spatial Varying Vectorial Holography and Polarization Encryption Based on Birefringent Metasurface," *Advanced Functional Materials* 34, no. 41 (2024): 2404196, https://doi.org/10.1002/adfm.202404196.

10. Z. Ji, Q. Chen, X. Sha, et al., "Multidimensional Multiplexing Metalens for STED Microscopy," *Science Advances* 11, no. 17 (2025): adt2807, https://doi.org/10.1126/sciadv.adt2807.

11. Z. Zhao, Z. Wang, Y. Shi, S. Wan, and Z. Li, "Multidimensional-Encrypted Meta-Optics Storage Empowered by Diffraction-Order Decoupling," *Advanced Materials* 37 (2025): 2419322, https://doi.org/10.1002/adma.202419322.

12. K. Kumar, H. Duam, R. S. Hegde, S. C. W. Koh, and J. N. Wei, "Printing Colour at the Optical Diffraction Limit," *Nature Nanotechnology* 7 (2012): 557–561, https://doi.org/10.1038/nnano.2012.128.

13. S. D. Rezaei, R. J. H. Ng, Z. Dong, et al., "Wide-gamut Plasmonic Color Palettes With Constant Subwavelength Resolution," *ACS Nano* 13 (2019): 3580–3588, https://doi.org/10.1021/acsnano.9b00139.

14. C. U. Hail, G. Schnoering, M. Damak, D. Poulikakos, and H. Eghlidi, "A Plasmonic Painter's Method of Color Mixing for a Continuous Red–Green–Blue Palette," *ACS Nano* 14 (2020): 1783–1791, https://doi.org/10.1021/acsnano.9b07523.

15. F. Neubrech, X. Duan, and N. Liu, "Dynamic Plasmonic Color Generation Enabled by Functional Materials," *Science Advances* 6 (2020): abc2709, https://doi.org/10.1126/sciadv.abc2709.

16. A. M. Shaltout, J. Kim, A. Boltasseva, V. M. Shalaev, and A. V. Kildishev, "Ultrathin and Multicolour Optical Cavities With Embedded Metasurfaces," *Nature Communications* 9 (2018): 2673, https://doi.org/10.1038/s41467-018-05034-6.

17. W.-J. Joo, J. Kyoung, M. Esfandyarpour, et al., "Metasurface-Driven OLED Displays Beyond 10000 Pixels Per Inch," *Science* 370 (2020): 459–463.

18. J. Proust, F. Bedu, B. Gallas, I. Ozerov, and N. Bonod, "All-Dielectric Colored Metasurfaces With Silicon Mie Resonators," *ACS Nano* 10, no. 8 (2016): 7761–7767, https://doi.org/10.1021/acsnano.6b03207.

19. X. Shang, G. He, L. Li, et al., "Controlling Brightness in Full Color Nanoprinting by All-Dielectric Metasurfaces," *Applied Physics Letters* 122 (2023): 181701, https://doi.org/10.1063/5.0143215.

20. J. Jang, T. Badloe, Y. Yang, T. Lee, J. Mun, and J. Rho, "Spectral Modulation Through the Hybridization of Mie-scatterers and Quasi-Guided Mode Resonances: Realizing Full and Gradients of Structural Color," *ACS Nano* 14, no. 11 (2020): 15317–15326, https://doi.org/10.1021/acsnano.0c05656.

21. M. Miyata, M. Nakajima, and T. Hashimoto, "High-sensitivity Color Imaging Using Pixel-Scale Color Splitters Based on Dielectric Metasurfaces," *ACS Photonics* 6 (2019): 1442–1450, https://doi.org/10.1021/acsphotonics.9b00042.

22. J.-H. Yang, V. E. Babicheva, M.-W. Yu, T.-C. Lu, T.-R. Lin, and K.-P. Chen, "Structural Colors Enabled by Lattice Resonance on Silicon Nitride Metasurfaces," *ACS Nano* 14 (2020): 5678–5685.

23. L. Wang, T. Wang, R. Yan, et al., "Color Printing and Encryption With Polarization-switchable Structural Colors on All-Dielectric Metasurfaces," *Nano Letters* 23 (2023): 5581–5587, https://doi.org/10.1021/acs.nanolett.3c01007.

24. S. Sun, Z. Zhou, C. Zhang, et al., "All-Dielectric Full-Color Printing With TiO_2 Metasurfaces," *ACS Nano* 11 (2017): 4445–4452, https://doi.org/10.1021/acsnano.7b00415.

25. B. Yang, W. Liu, Z. Li, et al., "Ultrahighly Saturated Structural Colors Enhanced by Multipolar-Modulated Metasurfaces," *Nano Letters* 19 (2019): 4221–4228, https://doi.org/10.1021/acs.nanolett.8b04923.

26. J. Eaves-Rathert, E. Kovalik, C. Fabian Ugwu, B. R. Rogers, C. L. Pint, and J. G. Valentine, "Dynamic Color Tuning With Electrochemically Actuated TiO_2 Metasurfaces," *Nano Letters* 22, no. 4 (2022): 1626–1632, https://doi.org/10.1021/acs.nanolett.1c04613.

27. Y. Li, J. Yin, C. Zhang, et al., "All-Dielectric Schrodinger Colours Across the Visible Spectrum," *Nature Communications* 16 (2025): 6990, https://doi.org/10.1038/s41467-025-66990-4.

28. E. Arbabi, S. M. Kamali, A. Arbabi, and A. Faraon, "Full-Stokes Imaging Polarimetry Using Dielectric Metasurfaces," *ACS Photonics* 5 (2018): 3132–3140, https://doi.org/10.1021/acsphotonics.8b00362.

29. Z. Yang, Z. Wang, Y. Wang, et al., "Generalized Hartmann-Shack Array of Dielectric Metalens Sub-Arrays for Polarimetric Beam Profiling," *Nature Communications* 9 (2018): 4607, https://doi.org/10.1038/s41467-018-07056-6.

30. A. Basiri, X. Chen, J. Bai, et al., "Nature-inspired Chiral Metasurfaces for Circular Polarization Detection and Full-Stokes Polarimetric Measurements," *Light: Science & Applications* 8 (2019): 78, https://doi.org/10.1038/s41377-019-0184-4.

31. C. Chen, X. Xiao, X. Ye, et al., "Neural Network Assisted High-Spatial-Resolution Polarimetry With Non-Interleaved Chiral Metasurfaces," *Light: Science & Applications* 12 (2023): 288, https://doi.org/10.1038/s41377-023-01337-6.

32. M. Song, D. Wang, Z. A. Kudyshev, et al., "Enabling Optical Steganography, Data Storage, and Encryption With Plasmonic Colors," *Laser & Photonics Reviews* 15 (2021): 2000343, https://doi.org/10.1002/lpor.202000343.

33. B. Xiong, Y. Liu, Y. Xu, et al., "Breaking the Limitation of Polarization Multiplexing in Optical Metasurfaces With Engineered Noise," *Science* 379 (2023): ade5140, https://doi.org/10.1126/science.ade5140.

34. Q. Huang, Z. Wang, Y. Shi, C. Xu, and Z. Li, "Toward Ultra-High-Capacity Meta-Optics Storage: 3D Data Cube Encrypted via Arbitrary Spatial Coordinates," *Advanced Functional Materials* 36 (2025): 12017.

35. Y. Xiao, L. Chen, M. Pu, et al., "Improved Spatiotemporal Resolution of Anti-scattering Super-Resolution Label-Free Microscopy via Synthetic Wave 3D Metalens Imaging," *Opto-Electronic Science* 2 (2023): 230037.

36. S. Chen, Y. Ha, F. Zhang, et al., "Towards the Performance Limit of Catenary Meta-optics via Field-driven Optimization," *Opto-Electronic Advances* 7 (2024): 230145, https://doi.org/10.29026/oea.2024.230145.

37. X. Liang, Z. Zhou, Z. Li, et al., "All-Optical Multiplexed Meta-Differentiator for Tri-Mode Surface Morphology Observation," *Advanced Materials* 35 (2023): 2301505, https://doi.org/10.1002/adma.202301505.

38. Q. Wang, Y. Fang, Y. Meng, et al., "Vortex-field Enhancement Through High-Threshold Geometric Metasurface," *Opto-Electronic Advances* 7, no. 12 (2024): 240112, https://doi.org/10.29026/oea.2024.240112.

39. E. Choi, G. Kim, and J. Yun, "360° Structured Light With Learned Metasurfaces," *Nature Photonics* 18 (2024): 848–855, https://doi.org/10.1038/s41566-024-01450-x.

40. M. Song, X. Li, M. Pu, et al., "Color Display and Encryption With a Plasmonic Polarizing Metamirror," *Nanophotonics* 7, no. 1 (2018): 323–331, https://doi.org/10.1515/nanoph-2017-0062.

41. Y. Bao, Y. Yu, H. Xu, et al., "Full-colour Nanoprint-hologram Synchronous Metasurface With Arbitrary Hue-saturation-brightness Control," *Light: Science & Applications* 8 (2019): 95, https://doi.org/10.1038/s41377-019-0206-2.

42. P. Huo, M. Song, W. Zhu, et al., "Photorealistic Full-Color Nanopainting Enabled by a Low-loss Metasurface," *Optica* 7, no. 9 (2020): 1171–1172, https://doi.org/10.1364/OPTICA.403092.

43. M. Song, L. Feng, P. Huo, et al., "Versatile Full-colour Nanopainting Enabled by a Pixelated Plasmonic Metasurface," *Nature Nanotechnology* 18 (2023): 71–72, https://doi.org/10.1038/s41565-022-01256-4.

44. T. Kaelberer, V. A. Fedotov, N. Papasimakis, D. P. Tsai, and N. I. Zheludev, "Toroidal Dipolar Response in a Metamaterial," *Science* 330 (2010): 1510–1512, https://doi.org/10.1126/science.1197172.

Supporting Information

Additional supporting information can be found online in the Supporting Information section.

Supporting File: adfm75615-sup-0001-SuppMat.docx.